A Unified Reconstruction Framework for Both Parallel-Beam and Variable Focal-Length Fan-Beam Collimators by a Cormack-Type Inversion of Exponential Radon Transform

Jiangsheng You,* *Member, IEEE,* Zhengrong Liang, *Member, IEEE,* and Gengsheng L. Zeng, *Member, IEEE*

***Abstract*—A variety of inversions of exponential Radon transform has been derived based on the circular harmonic transform in Fourier space by several research groups. However, these inversions cannot be directly applied to deal with the reconstruction for fan-beam or variable-focal-length fan-beam collimator geometries in single photon emission computed tomography (SPECT). In this paper, we derived a Cormack-type inversion of the exponential Radon transform by employing the circular harmonic transform directly in the projection space and the image space instead of the Fourier space. Thus, a unified reconstruction framework is established for parallel-, fan-, and variable-focal-length fan-beam collimator geometries. Compared to many existing algorithms, the presented one greatly mitigates the difficulty of image reconstruction due to the complicated collimator geometry and significantly reduces the computational burden of the special functions, such as Chebyshev or Bessel functions. By the well-established fast-Fourier transform (FFT), our algorithm is very efficient, as demonstrated by several numerical simulations.**

***Index Terms*—Circular harmonic decomposition, inverse exponential Radon transform, variable-focal-length fan-beam geometry.**

I. Introduction

QUANTITATIVE single photon emission computed tomography (SPECT) requires that photon attenuation within the body be compensated. When the attenuation in the region of interest (ROI) is uniformly distributed, both projection and reconstruction can be studied in the framework of exponential Radon transform [1]. An explicit inversion formula of the exponential Radon transform was first derived by Tretiak and Metz in two dimensions for parallel-beam collimator geometry [1]. Later, some alternative inversion algorithms were developed [2]–[10]. Since the Fourier transform (FT) of the sinogram, including certain convolutional forms as investigated in [9] and [10], was required in these studies, these inversion algorithms could not be directly applied to reconstruct images from projections acquired by nonparallel-beam collimator geometries unless a rebinning process was performed to interpolate the nonparallel-beam projections into parallel-beam projections. Weng *et al.* attempted to extend the filtered backprojection (FBP) algorithm in [1] to fan-beam collimator geometry by a coordinate transform [11], but this coordinate-transformed inversion could not preserve the FBP operation. Therefore, its implementation was complicated and required intensive computation. If the collimator geometry becomes more complicated than a fan-beam geometry, for example the variable-focal-length fan-beam types as discussed in [12], a direct extension of an FBP algorithm would become much more complicated and would require extremely intensive computations.

Circular harmonic decomposition was first used by Cormack to study the problem of reconstruction from projections [13]. The potential use of this technique to reconstruction of variable-focal-length fan-beam collimator projections was observed in our previous work [12]. In this paper, we extend the technique of circular harmonic decomposition to deal with the reconstruction in variable-focal-length fan-beam collimator geometry with the uniform attenuation correction. In this extension, the projection data are first decomposed into a Fourier-series expansion with respect to the angular variable. By the FBP inversion of the exponential Radon transform in [1], an explicit relation between the circular harmonic coefficients of the projection data and of the object image is then established. Image reconstruction for variable-focal-length fan-beam collimator geometry is, therefore, feasible. It should be pointed out here that the presented circular harmonic decomposition is conducted directly in both the projection space and the object-image space, rather than in the Fourier space as studied in [1], [2], and [5]–[8]. Our approach produces a simple unified algorithm for both parallel- and variable-focal-length fan-beam collimator geometries.

This paper is organized as follows. In Section II, the basic notation is introduced. In Section III, a brief review of the inverse exponential Radon transform is given. An alternative inversion by harmonic decomposition in both the projection space and the object space is then derived. The application of this newly developed inversion for the reconstruction of variable-focal-length fan-beam projections is investigated in

Manuscript received July 29, 1997; revised December 21, 1998. This work was supported in part by NIH under Grants HL51466 and NS33853 and in part by EI awards from the American Heart Association. The Associate Editor responsible for coordinating the review of this paper and recommending its publication was A. K. Louis. *Asterisk indicates corresponding author.*

*J. You and Z. Liang are with the Department of Radiology, State University of New York, Stony Brook, NY 11794 USA.

G. L. Zeng is with the Department of Radiology, University of Utah, Salt Lake City, UT 84108-1218 USA.

Publisher Item Identifier S 0278-0062(99)02027-3.

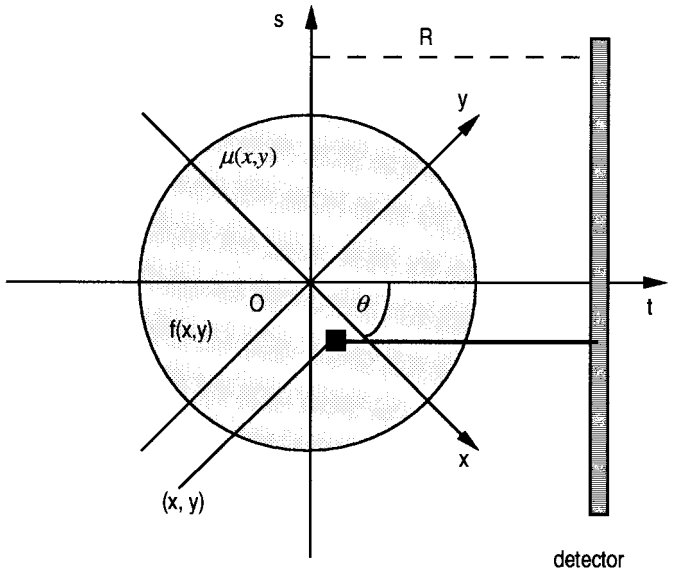

Fig. 1. The stationary coordinate systems (x, y), the rotating coordinate (s, t), and the detector location.

Section IV. Finally, several numerical simulations are performed to test the efficiency of the presented algorithm.

II. Basic Notation

The notations of [1] will be used throughout this paper. A point in the Euclidean space R^2 is denoted by a pair (x, y) or by a vector $\boldsymbol{r}$ $(\boldsymbol{r} = (x, y))$ in the Cartesian coordinate system or by a pair (r, φ) in the polar coordinate system. Let $f(x, y)$ denote the object function to be reconstructed and $f_\theta(s, t)$ $(f_\theta(s, t) = f(s\cos\theta - t\sin\theta, s\sin\theta + t\cos\theta))$ be the same object function expressed in the rotated Cartesian coordinate system (s, t) which is rotated from (x, y) system by an angle θ (see Fig. 1). The relation between these two coordinate systems is expressed as

$$\begin{pmatrix} s \\ t \end{pmatrix} = \begin{pmatrix} \cos\theta & \sin\theta \\ -\sin\theta & \cos\theta \end{pmatrix} \begin{pmatrix} x \\ y \end{pmatrix} \tag{1}$$

or

$$\begin{pmatrix} x \\ y \end{pmatrix} = \begin{pmatrix} \cos\theta & -\sin\theta \\ \sin\theta & \cos\theta \end{pmatrix} \begin{pmatrix} s \\ t \end{pmatrix}. \tag{2}$$

For the sake of simplicity, we introduce the following unit vectors:

$$\boldsymbol{j} = (\cos\theta, \sin\theta)$$
$$\boldsymbol{k} = (-\sin\theta, \cos\theta)$$

and the imaginary symbol i

$$i = \sqrt{-1}.$$

In SPECT imaging $f(x, y)$ represents the distribution of radiotracer concentration inside the body. Before the γ photons (emitted from the radiotracer) arrive at the detector they are attenuated by the body with attenuation coefficient distribution $\mu(x, y)$. Let $p(s, \theta)$ be the projection datum at position s with projection angle θ then

$$p(s,\theta) = \int_{-\infty}^{\infty} f(x,y)a(x,y,s,\theta) \cdot \delta(s + x\sin\theta - y\cos\theta)\, dx\, dy \tag{3}$$

where

$$a(x,y,s,\theta) = \exp\left[-\int_{(x,y)}^{\text{detector}} \mu(x',y') \cdot \delta(s + x'\sin\theta - y'\cos\theta)\, dx'\, dy'\right] \tag{4}$$

denotes the accumulated attenuation factor along the half line $s + x'\sin\theta - y'\cos\theta = 0$ from point (x, y) to the detector. In some applications, such as quantitative brain SPECT, $\mu(x, y)$ can be approximated as a constant μ in a convex region containing nonzero $f(x, y)$. In these cases, we define

$$b(s,\theta) = \exp[\mu L(s,\theta)] \tag{5}$$

where $L(s, \theta)$ is the distance from point $(s, 0)$ to the boundary point in the coordinate (s, t) with $t > 0$. Let $P_\mu f(s, \theta) = b(s, \theta)p(s, \theta)$ then $P_\mu f(s, \theta)$ is the exponential Radon transform of $f(x, y)$ expressed as

$$P_\mu f(s,\theta) = \int_{-\infty}^{\infty} f_\theta(s,t)e^{2\pi\mu_0 t}\, dt \tag{6}$$

where $\mu_0 = \mu/2\pi$.

Equation (6) implies that the modified projection $P_\mu f(s, \theta)$ is the exponential Radon transform of $f(x, y)$. The aim of this paper is to develop an efficient algorithm to reconstruct a function from its exponential Radon transform.

III. Reconstruction for Parallel-Beam Collimator Geometry

In this section we first give a quick review of Tretiak and Metz's method [1]. Let $\tilde{P}_\mu f(\omega, \theta)$ be the one-dimensional (1-D) FT of $P_\mu(s, \theta)$ with respect to the variable s, that is

$$\tilde{P}_\mu f(\omega,\theta) = \int_{-\infty}^{\infty} P_\mu f(s,\theta)e^{-2\pi i s\omega}\, ds. \tag{7}$$

Define

$$A^\varepsilon(\omega) = \exp(-\varepsilon^2(\omega^2 - \mu_0^2)) \tag{8}$$

$$H(\omega) = \begin{cases} |\omega|/2 & |\omega| \geq \mu_0 \\ 0 & |\omega| < \mu_0 \end{cases} \tag{9}$$

$$H^\varepsilon(\omega) = A^\varepsilon(\omega)H(\omega) \tag{10}$$

and

$$\tilde{P}_\mu^\varepsilon f(\omega,\theta) = H^\varepsilon(\omega)\tilde{P}_\mu f(\omega,\theta) \tag{11}$$

where ε is a positive number. Equation (11) can be rewritten in the spatial domain as

$$P_\mu^\varepsilon f(p,\theta) = \int_{-\infty}^{\infty} w^\epsilon(p-s)P_\mu f(s,\theta)\, ds \tag{12}$$

where

$$w^{\epsilon}(s) = \int_{-\infty}^{\infty} H^{\varepsilon}(\omega) e^{2\pi i \omega s}\, d\omega. \tag{13}$$

By performing a weighted backprojection of $P_{\mu}^{\varepsilon} f(p,\theta)$, a function $f_1(\boldsymbol{r})$ is obtained as

$$f_1(\boldsymbol{r}) = \int_0^{2\pi} P_{\mu}^{\varepsilon} f(\boldsymbol{r}\cdot\boldsymbol{j},\theta)\, \exp(-2\pi\mu_0 \boldsymbol{r}\cdot\boldsymbol{k})\, d\theta. \tag{14}$$

It is shown in the Appendix that

$$f_1(\boldsymbol{r}) = \iint_{R^2} f(\boldsymbol{z})\, d\boldsymbol{z} \cdot \int_{\mu_0}^{\infty} 2H^{\varepsilon}(\omega) J_0(2\pi|\boldsymbol{z}-\boldsymbol{r}|\sqrt{\omega^2-\mu_0^2})\, d\omega \tag{15}$$

where $J_0(\cdot)$ is the zeroth-order Bessel function and $\boldsymbol{z}$ denotes a vector in R^2. According to the properties of Hankel transform (for details see [1, App.]) we get

$$f_1(\boldsymbol{r}) = \iint_{R^2} f(\boldsymbol{z}) h(\boldsymbol{r}-\boldsymbol{z})\, d\boldsymbol{z} \tag{16}$$

where $h(\boldsymbol{r}-\boldsymbol{z}) = (1/2\varepsilon^2)\, \exp(-(\pi|\boldsymbol{r}-\boldsymbol{z}|^2/\varepsilon^2))$. Letting $\varepsilon \to 0$ we have $h(\boldsymbol{r}-\boldsymbol{z}) \to \delta(\boldsymbol{r}-\boldsymbol{z})$ and consequently $f_1(x,y) \to f(x,y)$. Here, the convergence could be understood in the sense of integral or continuity norm.

The above reconstruction procedure can be summarized in following steps.

Step 1: Filter the projection data in the frequency domain $\tilde{P}_{\mu}^{0}\, f(\omega,\theta) = H(\omega)\tilde{P}_{\mu}^{0} f(\omega,\theta)$.

Step 2: Find the inverse Fourier transform $P_{\mu}^{0} f(p,\theta) = \int_{-\infty}^{\infty} \tilde{P}_{\mu}^{0} f(\omega,\theta) e^{2\pi i\omega p}\, d\omega$.

Step 3: Backproject with an exponential weighting function to obtain the final image $f(\boldsymbol{r}) = \int_0^{2\pi} P_{\mu}^{0} f(\boldsymbol{r}\cdot\boldsymbol{j},\theta)\, \exp(-2\pi\mu_0\boldsymbol{r}\cdot\boldsymbol{k})\, d\theta$.

In clinical SPECT imaging the projection can be approximated to be band limited. Let $W(\omega)$ be the frequency window, that is, $W(\omega) = 1$ if ω is within the bandwidth, and zero elsewhere. In this case the filter function $H(\omega)$ can be replaced by $H(\omega)W(\omega)$ whose inverse FT exists and is denoted by $h(p)$. Thus, Step 1 can be implemented in the spatial domain as a convolution [3], i.e., a convolution backprojection algorithm can be obtained as

$$f(r,\varphi) = \int_0^{2\pi} \exp(-2\pi\mu_0 \boldsymbol{r}\cdot\boldsymbol{k})\, d\theta \cdot \int_{-\infty}^{\infty} h(r\cos(\theta-\varphi)-s) P_{\mu} f(s,\theta)\, ds. \tag{17}$$

In order to formulate a unified reconstruction method for both parallel- and variable-focal-length fan-beam collimator geometries, the circular harmonic decomposition expression of (17) will be given below.

Expanding $f(r,\varphi)$ and $P_{\mu} f(s,\theta)$ as their Fourier series with respect to the corresponding angular variables we have

$$f(r,\varphi) = \sum_{-\infty}^{\infty} f_n(r) e^{in\varphi} \tag{18}$$

and

$$P_{\mu} f(s,\theta) = \sum_{-\infty}^{\infty} P_n(s) e^{in\theta}. \tag{19}$$

To reconstruct $f(r,\varphi)$ from $P_{\mu} f(s,\theta)$ using (18) and (19) the key step is to establish a relation between $f_n(r)$ and $P_n(s)$. In the past, various relations between $f(r,\varphi)$ and $P_{\mu} f(s,\theta)$ were established in the Fourier space (see [1], [2], and [5]–[8]). To our knowledge, reconstructions using an explicit relation between $f_n(r)$ and $P_n(s)$ have not been investigated previously for attenuated Radon transform.

From (17) we have (see Appendix)

$$f_n(r) = \int_{-\infty}^{\infty} h_n(r,s) P_n(s)\, ds \tag{20}$$

where $h_n(r,s) = \int_0^{2\pi} e^{-in\varphi} h(r\cos\varphi - s) e^{-2\pi\mu_0 r\sin\varphi}\, d\varphi$. Unlike the kernel function in conventional FBP algorithm, here $h(\cdot)$ involves the uniform attenuation coefficient μ_0. The numerical implementation of (20) is simple because $h_n(r,s)$ can be computed by the fast-Fourier transform (FFT). Equation (20) will be called a Cormack-type inversion of the exponential Radon transform. It can be shown (see Appendix) that without the assumption that the projection is band limited (20) is

$$f_n(r) = \int_{-\infty}^{\infty} K_n(r,s) P_n(s)\, ds \tag{21}$$

where $K_n(r,s) = \int_0^{\infty} J_n(2\pi\rho r)(\sqrt{\rho^2+\mu_0^2} + \mu_0/\rho)^n e^{-2\pi i s\sqrt{\rho^2+\mu_0^2}}\, \rho\, d\rho$. The computation of $K_n(r,s)$ requires the calculations of Bessel functions and is not recommended for SPECT applications.

IV. Reconstruction for Variable-Focal-Length Fan-Beam Collimator Geometry

In SPECT imaging, a fan-beam collimator with variable focal lengths can be used with a gamma camera to improve detection efficiency and to reduce reconstruction artifacts due to truncation of projection data. The focal lengths increase from a minimum at the center to a maximum at the edge of the object (see Fig. 2). Thus, those projection rays with short focal lengths improve detection efficiency in the central ROI and others with long focal lengths avoid truncation artifacts near the edge of the object.

Assume that the flat detector is parallel to the y axis with a distance R away from the origin (see Fig. 2). The detected value at a point A on the detector is the integral of radionuclide distribution $f(x,y)$ along line SA where S is located on the x-axis. Let α denote the angle between line SA and the x axis. The focal point S has a varying distance $D(\alpha)$ from the origin. When the focal length increases from a minimum for rays passing through the center to a maximum for rays passing through the edge of the object $D(\alpha)$ should increase with $|\alpha|$. Every projection ray in Fig. 2 can be determined uniquely by angle α.

After the detector is rotated around the origin from the position of Fig. 2 by an angle Φ every point on the detector can be uniquely determined by either angular coordinate (Φ,α)

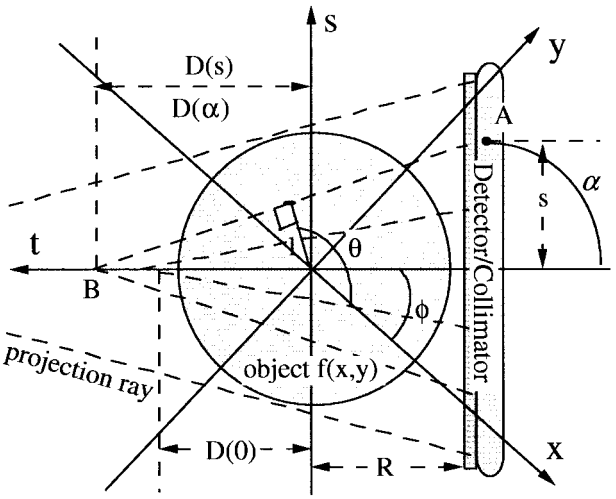

Fig. 2. Illustration of the variable-focal-length fan-beam geometry. The focal length $D(\cdot)$ can be expressed by either the angular coordinate α or the distance coordinate s. $D(\alpha)$ varies slowly near $\alpha = 0$ and changes fast when $|\alpha|$ increases.

or distance coordinate (Φ, s). Comparing with the parallel-beam coordinate (l, θ) we have the following relations for the angular coordinate:

$$l = D(\alpha)\ \sin\alpha \quad \text{and} \quad \theta = \Phi + \frac{\pi}{2} + \alpha. \tag{22}$$

The Jacobian from $d\alpha\ d\Phi$ to $dl\ d\theta$ is

$$J(\alpha) = D'(\alpha)\ \sin\alpha + D(\alpha)\ \cos\alpha \tag{23}$$

where $D'(\alpha)$ is the derivative of $D(\alpha)$ with respect to α.

Let $Pf(\Phi, \alpha)$ denote the measured projection datum at point (Φ, α) on the detector and $p(l, \theta)$ specify its corresponding expression in parallel-beam geometry. Multiplying $Pf(\Phi, \alpha)$ by the factor $b(l, \theta)$, defined in Section II, the modified projection data $P_\mu f(\Phi, \alpha)$ is the exponential Radon transform of $f(x, y)$ along some specifically arranged projection rays.

Because there exists a one-to-one mapping between $P_\mu f(\Phi, \alpha)$ and $P_\mu f(s, \theta)$, the reconstruction for variable-focal-length fan-beam collimator geometry should have the same accuracy as the reconstruction for the parallel-beam collimator geometry. By a translation property of the Fourier series, the coefficients $P_n(s)$ can be easily computed from the variable-focal-length fan-beam projection data $P_\mu f(\Phi, \alpha)$

$$P_n(D(\alpha)\ \sin\alpha) = e^{-in((\pi/2)+\alpha)} \int_0^{2\pi} P_\mu f(\Phi, \alpha) e^{in\Phi}\ d\Phi. \tag{24}$$

The coordinate transform (22) is a one-to-one mapping and the coefficients $P_n(l)$ in (20) can be obtained from (24) through phase translation. Similar to the proposed reconstruction procedure in [12], we summarize the above arguments and provide the following reconstruction steps.

1) Compute the FFT $\overline{P}_\mu f(n, \alpha)$ of $P_\mu f(\Phi, \alpha)$ with respect to the variable Φ for every fixed α.
2) Translate $\overline{P}_\mu f(n, \alpha)$ to $P_n(D(\alpha)\ \sin\alpha)$ by multiplying the factor $e^{-i((\pi/2)+\alpha)n}$.

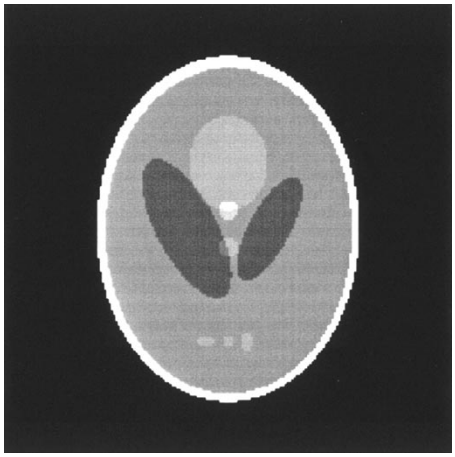

Fig. 3. Shepp–Logan phantom used for generating the projection data.

3) Compute the FFT $h_n(r, l)$ of kernel function $h(r\ \cos\varphi - l)e^{2\pi\mu_0 r\ \sin\varphi}$ with respect to the variable φ and multiply it to $P_n(l)$.
4) Compute the numerical integral of $h_n(r, l)P_n(l)$ with respect to the variable $l = D(\alpha)\ \sin\alpha$, then $f_n(r)$ are obtained.
5) By Fourier-series expansion $f(r, \varphi)$ is readily calculated from $f_n(r)$.
6) Finally, transform the polar coordinate expression $f(r, \varphi)$ to Cartesian coordinate expression $f(x, y)$.

V. Computer Simulations

In order to investigate the presented algorithm and show its efficiency, several simulations were performed. In these simulations, projection data of the Shepp–Logan phantom were analytically generated and discretely sampled. The phantom and the reconstructed images were shown by 200 × 200 digitizations with 256 gray scales. The cutoff frequency window was chosen as the Shepp–Logan window, thus the kernel function $h(t)$ is expressed as

$$h(t) = \frac{1}{\pi^2\epsilon^2}\left(\frac{1+\sin\frac{\pi t}{\epsilon}}{1+\frac{2t}{\epsilon}} + \frac{1-\sin\frac{\pi t}{\epsilon}}{1-\frac{2t}{\epsilon}}\right) - \frac{\mu^2}{\pi^2}\left(\operatorname{sinc}^2\left(\frac{\mu t}{\pi}\right) - 2\operatorname{sinc}\left(\frac{2\mu t}{\pi}\right)\right) \tag{25}$$

where the parameter ϵ was chosen according to the cutoff frequency.

Phantom: The Shepp–Logan phantom consisted of nine elliptical disks, as shown in Fig. 3. The attenuation coefficient μ was chosen as $\mu = 0.15$ per pixel within the phantom to simulate soft tissue at 140 keV; the pixel size is 0.5 cm. The simulated exponential Radon transform $P_\mu(\Phi, \alpha)$ is then analytically computed from this phantom.

Simulation I: For 128 angles evenly spaced on a circular scanning orbit and each projection with 128 bins, we performed three simulations for three types of acquisition geometry: parallel-, fan-, and variable-focal-length fan-beam collimator geometries. In the simulation of nonparallel collimator projections the subtending angle of α is $[-(\pi/4), (\pi/4)]$

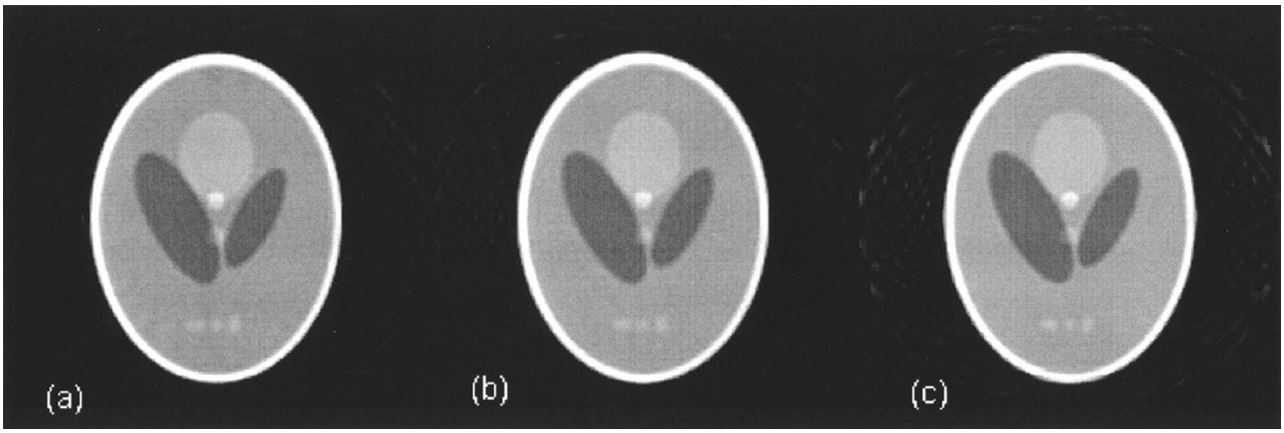

Fig. 4. The reconstructed images from 128 projections of 128 bins. The images (a)–(c) correspond to the parallel-, fan-, and variable fan-beam collimator geometries.

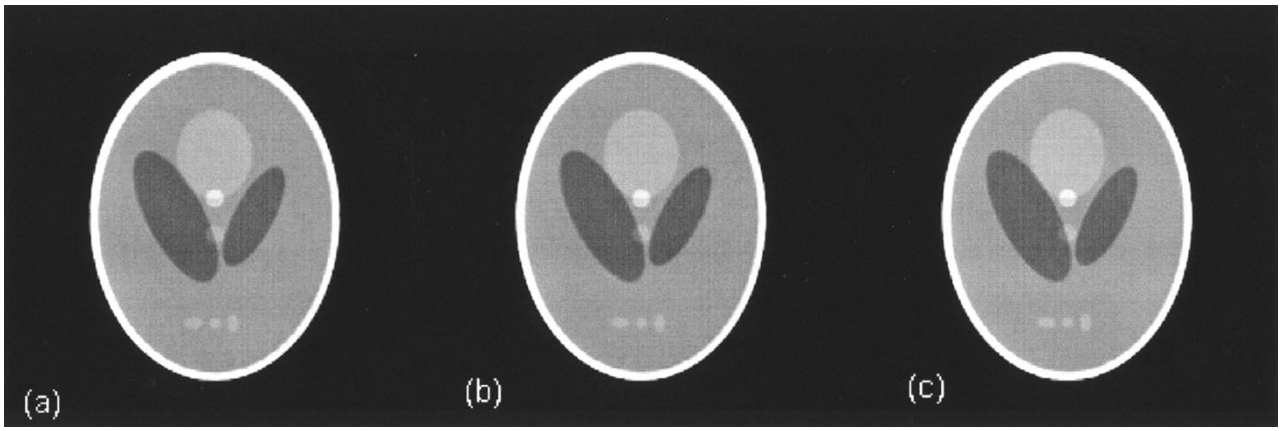

Fig. 5. The reconstructed images from 256 projections of 256 bins. The images (a)–(c) correspond to the parallel-, fan-, and variable fan-beam collimator geometries.

and Φ rotates from 0 to 2π. $D(\alpha) = 3.0$ (equivalent to 150-pixel size) for the fan-beam case and $D(\alpha) = (2/\cos(\alpha))$ ($D(0)$ is equivalent to 100-pixel size) for the variable focal-length fan-beam case. The reconstructed images are shown in Fig. 4(a)–(c) by 200 $\times$ 200 digitizations with 256 gray scales. The computation time was 10 s by a Pentium 266 PC for each of the three geometries.

Simulation II: For 256 projection angles each with 256 bins, we also performed three simulations for the three acquisition geometries. The reconstructed images are shown in Fig. 5(a)–(c) in the same size as before. The computation time was 80 s by the Pentium 266 PC for each geometry.

These simulations indicate that the proposed algorithm is efficient and the reconstructed images have the same quality for different collimator geometries. Other simulations (not shown in this paper) indicated that the presented algorithm is robust to a large extent of attenuation $0 \leq \mu < 2.0$. When μ is larger than two we need to sample the projection data denser in order to reduce the artifacts.

In the above simulations, noise was not included. This is due to two reasons. First, the presented algorithm is very similar to the conventional FBP algorithm for which the noise propagation in the reconstruction was thoroughly studied [8]. Our algorithm is only an implementation of FBP using circular harmonic decomposition. Second, the estimation theory in Sobolev space [14], [15] has given a quantitative description of the noise propagation in the projection and the reconstruction. A detailed study on the noise propagation in SPECT imaging is currently under investigation [16].

For clinical purposes, a typical application of the above theory is the brain SPECT. As shown in Fig. 6, it can be described as follows. The attenuation is from the brain and the skull bone, but the there is no radiotracer inside the skull, so after modification, the projection data can be changed to an exponential Radon transform, and then can be reconstructed by the proposed algorithm.

VI. Conclusion

Many reconstruction algorithms based on different inversions of the exponential Radon transform have been derived using Fourier-transformed sinograms [1], [2], [5]–[8]. These algorithms cannot be directly applied to deal with the reconstruction for fan-beam or variable-focal-length fan-beam collimator geometries unless the projections are rebinned into parallel data. We have developed a Cormack-type inversion of the exponential Radon transform for parallel-, fan-, and variable-focal-length fan-beam collimator geometries. This algorithm is an alternative to the conventional FBP algorithm

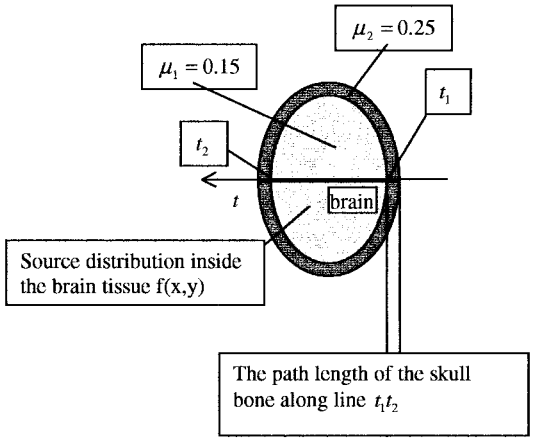

Fig. 6. The light black region denotes the brain tissues. The dark black region represents the skull and scalp with thickness of D along the black line t_1t_2. μ_1 and μ_2 denote the attenuation coefficients of the brain tissues and the skull bone, respectively. Along line t_1t_2 the detected projection datum can be expressed as $\int_{t_1}^{t_2} f(s,t)\ \exp((t-t_1)\mu_1 - D\mu_2)\ dt$. Then, we can obtain the exponential Radon transform $\int_{t_1}^{t_2} f(s,t)\ \exp(t\mu_1)\ dt$ by multiplying a factor $\exp(t_1\mu_1 + D\mu_2)$ to the acquired data.

through Fourier-series expansion. Its implementation is simple. The computation is efficient. It is expected that the presented algorithm will find applications in clinical SPECT imaging.

APPENDIX

The calculation of (15)

$$\begin{aligned}
f_1(\boldsymbol{r}) &= \int_0^{2\pi} \hat{P}_\mu^\varepsilon(\boldsymbol{r}\cdot\boldsymbol{j},\theta)\ \exp(-2\pi\mu_0\boldsymbol{r}\cdot\boldsymbol{k})\ d\theta \\
&= \int_0^{2\pi}\int_{-\infty}^{\infty} W^\varepsilon(\boldsymbol{r}\cdot\boldsymbol{j}-s) \\
&\quad \cdot \exp(-2\pi\mu_0\boldsymbol{r}\cdot\boldsymbol{k}) P_\mu(s,\theta)\ ds\ d\theta \\
&= \int_0^{2\pi} d\theta \int_{-\infty}^{\infty} ds \int_{-\infty}^{\infty} H^\varepsilon(\omega) e^{2\pi i\omega(\boldsymbol{r}\cdot\boldsymbol{j}-s)} \\
&\quad \cdot \exp(-2\pi\mu_0\boldsymbol{r}\cdot\boldsymbol{k})\ d\omega \\
&\quad \cdot \int_{-\infty}^{\infty} f(s\boldsymbol{j}+t\boldsymbol{k}) e^{2\pi\mu_0 t}\ dt \\
&= \int_0^{2\pi}\int_{-\infty}^{\infty} H^\varepsilon(\omega) e^{2\pi i\omega\boldsymbol{r}\cdot\boldsymbol{j} - 2\pi\mu_0\boldsymbol{r}\cdot\boldsymbol{k}}\ d\omega\ d\theta \\
&\quad \cdot \iint_{R^2} f(s\boldsymbol{j}+t\boldsymbol{k}) e^{2\pi\mu_0 t - 2\pi i\omega s}\ ds\ dt \\
&= \int_0^{2\pi}\int_{-\infty}^{\infty} H^\varepsilon(\omega) e^{2\pi i\omega\boldsymbol{r}\cdot\boldsymbol{j} - 2\pi\mu_0\boldsymbol{r}\cdot\boldsymbol{k}} \\
&\quad \cdot \iint_{R^2} f(\boldsymbol{z}) e^{2\pi\mu_0\boldsymbol{z}\cdot\boldsymbol{k} - 2\pi i\omega\boldsymbol{z}\cdot\boldsymbol{j}}\ d\boldsymbol{z} \\
&= \iint_{R^2} f(\boldsymbol{z})\ d\boldsymbol{z} \int_0^{2\pi}\int_{-\infty}^{\infty} H^\varepsilon(\omega) \\
&\quad \cdot e^{2\pi\mu_0(\boldsymbol{z}-\boldsymbol{r})\cdot\boldsymbol{k} - 2\pi i\omega(\boldsymbol{z}-\boldsymbol{r})\cdot\boldsymbol{j}}\ d\omega\ d\theta \\
&= \iint_{R^2} f(\boldsymbol{z})\ d\boldsymbol{z} \int_{\mu_0}^{\infty} 2H^\varepsilon(\omega)\ d\omega \\
&\quad \cdot \int_0^{2\pi} e^{2\pi\mu_0(\boldsymbol{z}-\boldsymbol{r})\cdot\boldsymbol{k} - 2\pi i\omega(\boldsymbol{z}-\boldsymbol{r})\cdot\boldsymbol{j}}\ d\theta \\
&\overset{\text{Appendix of [1]}}{=} \iint_{R^2} f(\boldsymbol{z})\ d\boldsymbol{z} \\
&\quad \cdot \int_{\mu_0}^{\infty} 2H^\varepsilon(\omega) J_0(2\pi|\boldsymbol{z}-\boldsymbol{r}|\sqrt{\omega^2-\mu_0^2})\ d\omega.
\end{aligned}$$

The calculation of (20)

$$\begin{aligned}
f_n(r) &= \int_0^{2\pi} f(r,\varphi) e^{-in\varphi}\ d\varphi \\
&= \int_{-\infty}^{\infty} ds \int_0^{2\pi} P_\mu(s,\theta)\ d\theta \\
&\quad \cdot \int_0^{2\pi} h(r\cos(\varphi-\theta)-s) \\
&\quad \cdot e^{-2\pi\mu_0\ \sin(\varphi-\theta)} e^{-in\varphi}\ d\varphi \\
&= \int_{-\infty}^{\infty} ds \int_0^{2\pi} P_\mu(s,\theta) e^{-in\theta}\ d\theta \\
&\quad \cdot \int_0^{2\pi} h(r\cos\varphi - s)) e^{-2\pi\mu_0\ \sin\varphi} e^{-in\varphi}\ d\varphi \\
&= \int_{-\infty}^{\infty} ds\ P_n(s) \\
&\quad \cdot \int_0^{2\pi} h(r\ \cos\varphi - s)) e^{-2\pi\mu_0 \sin\varphi} e^{-in\varphi}\ d\varphi.
\end{aligned}$$

The calculation of (21)

$$\begin{aligned}
f_n(r) &= \int_0^{2\pi} f(r,\varphi) e^{-in\varphi}\ d\varphi \\
&= \int_0^{\infty} \rho J_n(2\pi\rho r)\ d\rho \int_0^{2\pi} F(\rho,\Phi) e^{-in\Phi}\ d\Phi \\
&= \int_0^{\infty} J_n(2\pi\rho r) \left(\frac{\sqrt{\rho^2+\mu_0^2}+\mu_0}{\rho}\right)^n \rho\ d\rho \\
&\quad \cdot \int_{-\infty}^{\infty}\int_0^{2\pi} P_\mu f(s,\theta) \\
&\quad \cdot e^{-2\pi i s\sqrt{\rho^2+\mu_0^2}}\ ds\ d\theta \quad \text{by (33) of [1]} \\
&= \int_0^{\infty} \left(\frac{\sqrt{\rho^2+\mu_0^2}+\mu_0}{\rho}\right)^n J_n(2\pi\rho r)\ \rho\ d\rho \\
&\quad \cdot \int_0^{2\pi} \tilde{P}_\mu f(\sqrt{\rho^2+\mu_0^2},\theta)\ e^{-in\theta}\ d\theta \\
&= \int_0^{\infty} J_n(2\pi\rho r) \left(\frac{\sqrt{\rho^2+\mu_0^2}+\mu_0}{\rho}\right)^n \rho\ d\rho \\
&\quad \cdot \int_{-\infty}^{\infty} P_n(s) e^{-2\pi i s\sqrt{\rho^2+\mu_0^2}}\ ds \\
&= \int_{-\infty}^{\infty} P_n(s)\ ds \\
&\quad \cdot \int_0^{\infty} J_n(2\pi\rho r) \left(\frac{\sqrt{\rho^2+\mu_0^2}+\mu_0}{\rho}\right)^n \\
&\quad \cdot e^{-2\pi i s\sqrt{\rho^2+\mu_0^2}}\ \rho\ d\rho
\end{aligned}$$

where $F(\xi, \Phi)$ is the polar coordinate expression of the Fourier transform of the object function $f(r, \varphi)$ and $J_n(\cdot)$ denotes the nth-order Bessel function.

REFERENCES

[1] O. J. Tretiak and C. E. Metz, "The exponential Radon transform," *SIAM J. Appl. Math.*, vol. 39, pp. 341–354, 1980.

[2] S. Bellini, M. Piacentini, C. Cafforio and F. Rocca, "Compensation of tissue absorption in emission tomography," *IEEE Trans. Acoust. Speech, Signal Processing*, vol. 27, pp. 213–218, Feb. 1979.

[3] G. T. Gullberg and T. F. Budinger, "The use of filtering methods to compensate for constant attenuation in single photon emission computed tomography," *IEEE Trans. Biomed. Eng.*, vol. 28, pp. 142–157, Feb. 1981.

[4] A. V. Clough and H. H. Barrett, "Attenuated Radon and Abel transforms," *J. Opt. Soc. Am.*, vol. 73, pp. 1590–1595, 1983.

[5] A. Markoe, "Fourier inversion of the attenuated X-ray transform," *SIAM J. Math. Anal.*, vol. 15, pp. 718–722, 1984.

[6] T. Inouye, K. Kose, and A. Hasegawa, "Image reconstruction algorithm for single photon emission computed tomography with uniform attenuation," *Phys. Med. Biol.*, vol. 34, pp. 299–304, 1989.

[7] W. G. Hawkins, P. K. Leichner, and N. C. Yang, "The circular harmonic transform for SPECT reconstruction and boundary conditions on the Fourier transform of the sinogram," *IEEE Trans. Med. Imag.*, vol. 7, pp. 135–148, June, 1988.

[8] C. E. Metz and X. Pan, "A unified analysis of exact methods of inverting the 2-D exponential Radon transform, with implications for noise control in SPECT," *IEEE Trans. Med. Imag.*, vol. 17, pp. 643–658, Dec. 1995.

[9] I. A. Hazou and D. C. Solmon, "Inversion of the exponential X-ray transform I: Analysis," *Math. Meth. Appl. Sci.*, vol. 10, pp. 561–574, 1988.

[10] I. A. Hazou and D. C. Solmon, "Inversion of the exponential X-ray transform II: Numerics," *Math. Meth. Appl. Sci.*, vol. 13, pp. 205–218, 1990.

[11] Y. Weng, L. Zeng, and G. T. Gullberg, "Analytical inversion formula for uniformly attenuated fan-beam projections," *IEEE Trans. Nucl. Sci.*, vol. 44, pp. 243–249, Apr. 1997.

[12] J. You, Z. Liang, and S. Bao, "A harmonic decomposition reconstruction algorithm for spatially-varying focal length fan-beam collimators," *IEEE Trans. Med. Imag.*, vol. 17, Dec. 1998.

[13] A. M. Cormack, "Representations of a function by its line integrals, with some applications, II," *J. Appl. Phys.*, vol. 35, pp. 2908–2931, 1964.

[14] F. Natterer, *The Mathematics of Computerized Tomography*. New York: Wiley, 1986.

[15] U. Heike, "Single-photon emission computed tomography by inverting the attenuated Radon transform with least-squares collocation," *Inverse Problems*, vol. 2, pp. 307–330, 1986.

[16] J. You, G. Han, and Z. Liang, "A Poisson impulse field analysis on noise propagation in SPECT imaging," State Univ. NY, Stony Brook, Dept. Radiology, IRIS Lab Rep.